

Disentangling the Galactic binary zoo: Machine learning classification of stellar remnant binaries in LISA data

Irwin K. C. Tay¹, Valeriya Korol^{2, 1}, and Thibault Lechien¹

¹ Max-Planck-Institut für Astrophysik, Karl-Schwarzschild-Straße 1, 85748 Garching, Germany

² SRON Space Research Organisation Netherlands, Niels Bohrweg 4, 2333 CA Leiden, the Netherlands
e-mail: v.korol@sron.nl

March 9, 2026

ABSTRACT

The Laser Interferometer Space Antenna (LISA) will open a new observational window in the millihertz gravitational-wave band, enabling the detection of tens of thousands of compact stellar remnant binaries across the Milky Way. Most of LISA's sources will be double white dwarf (WDWD) systems, while neutron star–white dwarf (NSWD) binaries and higher-mass systems will be orders of magnitude rarer but of significant astrophysical interest. Disentangling these populations is challenging due to the strong overlap in their gravitational-wave features. In this work, we investigate the use of machine-learning techniques to classify LISA-detectable binaries based solely on LISA observables.

Using mock catalogues of Galactic binaries constructed from population-synthesis studies, we evaluate a range of machine-learning classifiers. We find that ensemble-based methods—particularly gradient-boosting algorithms such as XGBoost—deliver the best performance on our highly imbalanced dataset. WDWD systems are identified with a recall of $\sim 99\%$, reflecting their dominant presence, and high-mass binaries are also classified with high recall ($\geq 85\%$). In contrast, NSWD systems remain the most challenging population to distinguish: their features overlap strongly with those of WDWD binaries, making them particularly prone to misclassification. Despite this, XGBoost correctly identifies 85.6% of NSWD systems in our simulated LISA detections, outperforming simple statistical approaches based on kernel density estimation. We further demonstrate that machine-learning classification can effectively support the interpretation of LISA data, enabling the identification of eccentric binaries and extremely rare subclasses.

Key words. gravitational waves – white dwarfs – binaries (including multiple): close – stars: neutron

1. Introduction

The Laser Interferometer Space Antenna (LISA) is one of the European Space Agency's flagship missions, scheduled for launch in the 2030s (Colpi et al. 2024). It will open a new observational window in the gravitational-wave spectrum, between 0.1 mHz and 1 Hz, providing access to a new set of gravitational-wave sources: from compact stellar remnant binaries in our own Galaxy, to mergers of massive black holes across cosmic time, and to potential cosmological signals from the primordial Universe (for a review see Barausse et al. 2020; Auclair et al. 2023; Amaro-Seoane et al. 2023).

In this study, we consider Galactic gravitational-wave sources accessible to LISA—binary systems composed of white dwarfs, neutron stars, and black holes with orbital periods of less than a few hours. Among these, double white dwarf (WDWD) binaries are expected to be the most numerous by far (e.g. Nelemans et al. 2001). Theoretical studies predict that LISA will individually resolve approximately $O(10^4)$ WDWD binaries (e.g. Korol et al. 2017; Lamberts et al. 2019; Thiele et al. 2023; Li et al. 2023; Rajamuthukumar, Abinaya Swaruba et al. 2025). This is mainly due to two factors. First, the initial mass function favours the formation of low-mass stars, which later evolve into white dwarfs. Second, low-mass stars live much longer than their massive counterparts and therefore accumulate in the Galaxy over time. Comparatively, all other types of binaries are expected to be orders of magnitude less numerous: binaries composed of a neutron star and a white dwarf (NSWD) are expected to yield

$O(10^2)$ detections (e.g. Breivik et al. 2020; Chen et al. 2020; Korol et al. 2024a), while binaries containing two neutron stars (NSNS) or black holes (BHNS and BHBH) are predicted to be even rarer, with only $O(10)$ expected detections for each of these classes (e.g. Lamberts et al. 2018; Lau et al. 2020; Wagg et al. 2022; Tang et al. 2024). These latter systems are the products of massive stellar evolution and, owing to their short lifespans and the supernova kicks that can disrupt them, they tend to disappear from the Galaxy over time (e.g. Wagg et al. 2025).

These detections represent only the tip of the iceberg of the underlying Galactic population in the LISA frequency band. The diverse binary populations will together produce a complex gravitational-wave signal in the LISA band, composed of tens of millions of overlapping sources. Extracting the thousands of individually 'loud' signals mentioned above from the overall Galactic 'hum' represents one of the central challenges of LISA data analysis (e.g. Nissanke et al. 2012; Karnesis et al. 2021; Lackeos et al. 2023). Addressing this challenge is the first step in LISA's global fit analysis, which involves the simultaneous modelling and subtraction of multiple source types from the data stream (e.g. Littenberg & Cornish 2023; Strub et al. 2024; Katz et al. 2025; Deng et al. 2025).

Assuming that the LISA global fit successfully extracts and catalogues $O(10^4)$ individual Galactic gravitational-wave sources, a natural next question arises: given the overwhelming number of WDWD binaries, how easily, if at all, can the different types of binaries be distinguished from each other? This is a non-trivial task, since in the LISA band most binaries appear as

continuous, quasi-monochromatic sources. In the low-frequency regime ($f \lesssim 1\text{--}2$ mHz), their gravitational-wave signal is effectively monochromatic, showing no measurable frequency derivative (the so-called chirp); in this case only the amplitude and frequency can be determined from the LISA data alone. Without a chirp measurement, the chirp mass—the specific combination of the component masses that sets the frequency evolution—is degenerate with distance, making it virtually impossible to distinguish between, for example, a nearby WDWD binary and a more distant BHBH binary (e.g. [Sesana et al. 2020](#)). At higher frequencies ($f \gtrsim 1\text{--}3$ mHz), the frequency derivative becomes measurable, allowing one to infer bounds on binary component masses via the chirp mass measurement (e.g. [Korol et al. 2024a](#)). Recent studies by [Moore et al. \(2024\)](#) and [Middleton et al. \(2025\)](#) have further shown that, if the binary is eccentric, individual component masses can be constrained, at least in some cases. In eccentric systems, the orbit will undergo periastron precession, which introduces an additional modulation in the gravitational-wave signal. The associated precession frequency depends on the total mass of the binary, and if it can be measured together with the chirp mass, the degeneracy is broken and the individual component masses can be disentangled ([Seto 2001](#)). This is expected mainly in systems with a neutron star component, where natal kicks at birth can impart significant orbital eccentricity (e.g. [Popov et al. 2025](#); [Valli et al. 2025](#); [Vigna-Gómez 2025](#), and references therein).

Disentangling Galactic gravitational-wave sources is an essential first step in interpreting LISA data and is a necessary prerequisite for addressing binary-type-specific LISA science goals ([Colpi et al. 2024](#)). In this work, we investigate whether machine learning techniques can aid in overcoming the expected difficulties and enable accurate classification of Galactic stellar remnant binaries in LISA data. Specifically, we explore the use of machine learning algorithms for classifying multiple binary classes detectable by LISA. In addition, by focusing on two largely overlapping classes (WDWD and NSWD), we assess the strengths of these algorithms and compare their performance with that of a classical statistical approach based on the kernel density estimation (KDE). Finally, we discuss potential other applications of such classification that can advance LISA science.

The remainder of this paper is organised as follows. In Section 2, we describe the gravitational-wave parameters, the synthesis of the catalogues, and how they were used for training and testing our machine learning algorithms. We also outline the types of classifiers employed, the methods applied, and the metrics used to evaluate their performance. The main results are presented in Section 3, starting with those of the multi-class classifier, followed by an analysis of the performance of other classifiers in the binary classification study. In Section 4, we discuss the potential of extending this classification approach to other use cases in the LISA context. Finally, we conclude our work in Section 5.

2. Methods

In this section, we describe the definitions of the gravitational-wave features and astrophysical catalogues used for training and testing our classifiers. We then outline the classifiers employed in our study, along with the optimisation and probability calibration methods applied. Finally, we define the evaluation metrics used to assess the performance of our classifiers.

2.1. Binary's detectability with LISA

Consider a binary system with masses m_1 and m_2 and semi-major axis a . Kepler's law relates the orbital period to the total mass $M = m_1 + m_2$; expressed in terms of the gravitational-wave frequency:

$$f_{\text{GW}} = \frac{1}{\pi} \sqrt{\frac{GM}{a^3}} \quad (1)$$

$$= \left(\frac{M}{1 M_\odot}\right)^{1/2} \left(\frac{a}{1 R_\odot}\right)^{-3/2} \times 0.20 \text{ mHz}. \quad (2)$$

Gravitational-wave radiation causes the orbit to shrink, producing a gradual chirp of the frequency:

$$\dot{f}_{\text{GW}} = \frac{96}{5\pi c^5} (GM_c)^{5/3} (\pi f_{\text{GW}})^{11/3} \quad (3)$$

$$= \left(\frac{M_c}{1 M_\odot}\right)^{5/3} \left(\frac{f_{\text{GW}}}{1 \text{ mHz}}\right)^{11/3} \times 0.18 \text{ nHz year}^{-1}, \quad (4)$$

where M_c is the chirp mass. A binary's detectability with LISA is primarily determined by its GW strain amplitude:

$$\mathcal{A}_0 = \frac{2(GM_c)^{5/3} (\pi f_{\text{GW}})^{2/3}}{Dc^4} \quad (5)$$

$$= \left(\frac{M_c}{1 M_\odot}\right)^{5/3} \left(\frac{f_{\text{GW}}}{1 \text{ mHz}}\right)^{2/3} \left(\frac{10 \text{ kpc}}{D}\right) \times 5.94 \times 10^{-23}. \quad (6)$$

Since gravitational-wave instruments respond directly to the strain amplitude—rather than to flux, as in electromagnetic astronomy—the corresponding signal-to-noise ratio (SNR) over an observation time T_{obs} is

$$\langle \rho^2 \rangle \propto \frac{\mathcal{A}_0^2 T_{\text{obs}}}{S_n(f_{\text{GW}})}, \quad (7)$$

where $S_n(f)$ is LISA's noise spectral density defined in the [LISA Science Requirements Document \(2018\)](#).

Current LISA global fit pipelines model Galactic binaries using circular, quasi-monochromatic waveforms characterised by eight parameters:

$$\{f_{\text{GW}}, \dot{f}_{\text{GW}}, \mathcal{A}_0, \lambda, \beta, \iota, \psi, \phi_0\}, \quad (8)$$

where, in addition to the quantities defined above, (λ, β) are the sky coordinates, ι is the inclination, ψ the gravitational-wave polarisation angle, and ϕ_0 the initial orbital phase (see [Littenberg & Cornish 2023](#); [Strub et al. 2024](#); [Katz et al. 2025](#); [Deng et al. 2025](#)). These parameters are direct LISA observables and therefore form the core feature set used in our machine learning analysis. We also include the SNR (ρ) as an additional feature, as it will likely be reported in future LISA source catalogues and may carry useful information for training. Recent studies have begun to incorporate eccentricity into waveform models and parameter estimation of Galactic LISA sources (e.g. [Katz et al. 2022](#); [Moore et al. 2024](#); [Middleton et al. 2025](#)). Motivated by these studies and by the astrophysical importance of eccentricity, we include eccentricity e as an additional feature in our analysis.

For completeness, we note that, if the binary is eccentric, gravitational-wave radiation is emitted across multiple harmonics of the orbital frequency ([Peters & Mathews 1963](#)). Each harmonic contributes power at

$$f_n = n f_{\text{orb}} = \frac{n f_{\text{GW}}}{2}, \quad (9)$$

with strain amplitude

$$\mathcal{A}_n = \mathcal{A}_0 \left(\frac{2}{n}\right)^{5/3} \sqrt{g(n, e)}, \quad (10)$$

where $g(n, e)$ is defined in [Peters & Mathews \(1963\)](#). In this case, the total SNR is obtained by summing the SNRs of the detectable harmonics in quadrature.

2.2. Main catalogue of LISA-detectable Galactic binaries for training and testing

To train our machine learning classifiers, we construct a representative catalogue of Galactic sources detectable by LISA. Our catalogue combines white dwarf binaries (the ‘low-mass’ population of WDWD and NSWD) with neutron star and black hole binaries (the ‘high-mass’ population of NSNS, BHNS, BHBH), drawn from two separate published population studies. As a result, the populations are not generated within a single self-consistent framework; however, for the purpose of our exploratory work—focusing solely on disentangling binary types—this approach is sufficient. We ensure that the relative numbers of each binary class reflect astrophysically motivated, fiducial expectations for LISA detections.

The low-mass population, comprising the WDWD and NSWD binaries, is taken from our earlier work ([Korol et al. 2024b](#)). In that study, the populations were generated using the SeBa binary population synthesis code ([Portegies Zwart & Verbunt 1996](#); [Nelemans et al. 2001](#); [Toonen et al. 2012, 2018](#)), which is widely used for modelling low-mass binary evolution and is calibrated against observed samples ([Nelemans et al. 2000](#); [Nelemans & Tout 2005](#); [van der Sluys et al. 2006](#); [Toonen et al. 2017](#)). The population comprises a suite of nine variations, each based on different assumptions about binary interactions (specifically the treatment of common-envelope evolution) and the distribution of natal kicks imparted to neutron stars at birth. Since these binary classes are expected to constitute $\sim 99.9\%$ of the LISA-detectable Galactic population, they are the most critical to model self-consistently, particularly to separate individually detectable binaries from those that contribute to the unresolved Galactic foreground. For this purpose, all populations variations were processed through an iterative pipeline described in [Karnešis et al. \(2021\)](#), which approximates the LISA global fit analysis.

Based on the SNR threshold, the pipeline iteratively separates individually resolved (high- ρ) sources from the unresolved (low- ρ) Galactic population, allowing us to extract a subset of LISA-detectable binaries for each catalogue variation. We note that the pipeline employs purely circular waveforms. Given that a significant fraction ($\sim 45\%$) of NSWD binaries in our mock catalogues retain non-zero eccentricities, each eccentric NSWD catalogue entry is decomposed into a collection of harmonics (see Sect. 2.1), with the number of harmonics chosen to capture $\sim 99\%$ of the emitted energy. However, only up to several harmonics of a given binary are detectable across all mock catalogue variations (see Figure 4 of [Korol et al. 2024b](#)). We retain all detectable harmonics for training as they can be detected as separate individual sources, even though they remain physically correlated. The resulting low-mass component in the main catalogue of LISA detectable binaries contains a total of 50,255 binaries, of which 48,311 are WDWD systems and 1,944 are NSWD systems of which 1,410 of them are unique (i.e. not representing harmonics of the same eccentric NSWD system).

The high-mass population consists of NSNS, BHNS, and BHBH binaries drawn from the fiducial model of [Wagg et al.](#)

Table 1: Gravitational-wave features used for machine learning classification.

Parameter	Symbol	Units	Origin
GW frequency	f_{GW}	Hz	K24/W22
Frequency derivative	\dot{f}_{GW}	Hz/s	K24/W22
Amplitude	\mathcal{A}_0	—	K24/W22
Eccentricity	e	—	K24/W22
Signal-to-noise ratio	ρ	—	K24/W22
Ecliptic longitude	λ	rad	K24/W22
Ecliptic latitude	β	rad	K24/W22
Inclination angle	ι	rad	$\cos \iota \sim \mathcal{U}(-1, 1)$
Polarisation angle	ψ	rad	$\mathcal{U}(0, 2\pi)$
Initial phase	ϕ_0	rad	$\mathcal{U}(0, 2\pi)$

Notes. Values for f_{GW} , \dot{f}_{GW} , \mathcal{A} , e , λ , and β for the WDWD and NSWD binary classes are taken directly from the astrophysical catalogues of [Korol et al. \(2024b, K24\)](#), while the corresponding values for the NSNS, BHNS, and BHBH classes are taken from [Wagg et al. \(2022, W22\)](#). The remaining angular parameters are drawn assuming isotropy. Here, $\mathcal{U}(a, b)$ denotes a uniform distribution between a and b .

(2022), obtained using the COMPAS population synthesis code ([Broekgaarden et al. 2021, 2022](#); [Riley et al. 2022](#)). For each of these binary classes, we select a weighted random subset of systems according to the simulation weights. In [Wagg et al. \(2022\)](#), the fiducial population model predicts that, over a four-year (ten-year) LISA mission, at least 37 (70) BHBHs, 18 (38) BHNSs, and 5 (8) NSNSs would be distinguishable above the WDWD foreground. To preserve these relative proportions while ensuring sufficient training statistics, we inflate the absolute counts and sample (4,630; 2,630; 500) binaries for BHBH, BHNS, and NSNS respectively. This yields a dataset large enough for machine learning applications.

To preserve an astrophysically motivated, fiducial test set, we drew and reserved a representative subset of the high-mass binaries: 93 BHBH, 53 BHNS, and 10 NSNS systems (roughly matching the expected LISA detection counts from [Wagg et al. 2022](#)).

For the low-mass binaries, we reserved 20% for testing, resulting in 9,662 WDWD and 389 NSWD systems. We then combined the low- and high-mass populations. All remaining data (i.e., not reserved for testing) was split 80/20 into training and validation sets.

We summarise gravitational-wave parameters (features) used for the training in Table 1 and show the distribution of the features in the training data in Fig. 1. Finally, we note that the input features were standardised through z-score normalisation based on the training data, and the same transformation was applied to the validation and test sets to ensure consistency.

2.2.1. Other auxiliary catalogues

In addition to our main catalogue, we consider a single random realisation of the low-mass binary population, based on one of the astrophysical model variations included in the main catalogue. By construction, this realisation preserves the total number and relative proportions of each class expected from a realistic four-year LISA observation: 20,791 binaries in total, comprising 20,608 WDWD systems and 183 NSWD systems. Because this catalogue is used exclusively for performance evaluation, we will refer to it as the low-mass test catalogue.

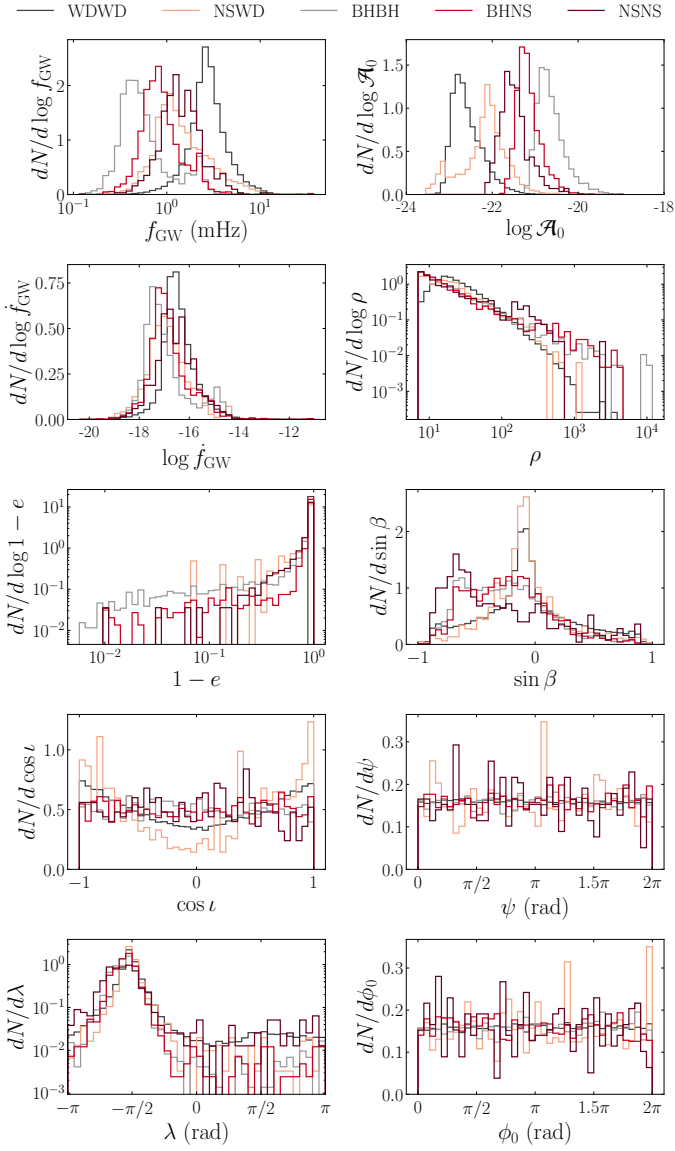


Fig. 1: Distributions of the ten features in the data used for the machine learning classifiers, coloured by true class. Black: WDWD binaries; orange: NSWD binaries; grey: BHBH binaries; red: BHNS binaries; and maroon: NSNS binaries. Each distribution is normalised independently.

We also consider an independent catalogue of low-mass binaries from [Korol et al. \(2022\)](#), which was also not used during training. Importantly, it contains only WDWD systems, with a total of 59,250 binaries. We use this catalogue to assess the classifier’s ability to correctly identify a population consisting solely of WDWD systems, and demonstrate robustness when applied to data derived from an unseen astrophysical model. This catalogue represents a stringent test of whether the classifier can generalise beyond the assumptions built into the training data.

As for the main catalogue, the input features in both auxiliary catalogues were also normalised using the transformation derived from the training data, and the same transformation is applied to the validation and test sets, to the low-mass test catalogue, and to the independent catalogue.

2.3. Machine learning classification methods

In this study, we adopt an explorative approach to identify the most suitable classifier for distinguishing among different types of compact binaries. To this end, we evaluate seven machine learning techniques, ranging from simple baseline models to more complex probabilistic and ensemble methods, and one simple statistical approach.

The classifiers used in our analysis are:

- K-Nearest Neighbour (KNN; [Silverman & Jones 1989](#); [Cover & Hart 1967](#)): One of the simplest machine learning classification techniques using a distance-based method, that provides a baseline for how well local neighbourhood information alone can separate classes.
- Support Vector Machine (SVM; [Cortes & Vapnik 1995](#)): Effective at finding separating hyperplanes in high-dimensional feature spaces, making it suitable for testing linear class boundaries.
- Random Forest (RF; [Breiman 2001](#)): An ensemble of decision trees that aims to reduce overfitting through bagging and random feature selection.
- Deep Neural Network (NN): A custom made flexible, high-capacity model that can capture complex, non-linear relationships between input and output parameters (for more details see [Appendix A.1](#)).
- Natural Gradient Boosting (NGBoost; [Duan et al. 2020](#)): A method for probabilistic prediction that produces calibrated uncertainty estimates.
- Gaussian Mixture Model (GMM): Each class is modelled as a mixture of multivariate Gaussian components in the feature space by maximising the likelihood of the training data for that class. We follow the implementation of [Bailer-Jones et al. \(2019\)](#) but incorporate our class priors to address class imbalance.
- XGBoost ([Chen & Guestrin 2016](#)): A highly optimized gradient-boosted decision tree algorithm known for its strong performance and efficiency across structured datasets, making it a natural candidate for our tabular features.

Details of the classifier implementations are provided in [Section A](#). All classifiers were optimised using Bayesian optimisation (see [Section A.2](#)), and their probabilistic outputs were calibrated using a Bayes’ rule-based method adapted from ([Berbel et al. 2024](#), for details see [Section A.3](#)).

We compare the classifiers listed above to a simple statistical approach to classification based on KDE combined with Bayes’ theorem. Let \mathcal{D} denote the training dataset consisting of ten gravitational-wave features \vec{x} listed in [Table 1](#). We used a Gaussian kernel, with the bandwidth selected via grid search. Specifically, we explored a logarithmically spaced range of values given by `np.logspace(-1, 1, 20)`, which yielded an optimal bandwidth of $h = 0.20691$. Using the KDE, we approximated the class-conditional densities. $\hat{p}(\vec{x} | y = 0)$ and $\hat{p}(\vec{x} | y = 1)$ where they represent the likelihood of class 0 and class 1 given a set of features \vec{x} respectively. Together with the empirical class priors π_0 and π_1 (in our case these are simply class ratio estimated from our catalogues), estimated from \mathcal{D} . Bayes’ theorem then yields the posterior probability for class 1:

$$P(y = 1 | \vec{x}) = \frac{\hat{p}(\vec{x} | y = 1)\pi_1}{\hat{p}(\vec{x} | y = 1)\pi_1 + \hat{p}(\vec{x} | y = 0)\pi_0}. \quad (11)$$

The posterior for class 0 follows analogously.

2.3.1. Evaluation metrics

When presenting our results, we use confusion matrices to illustrate the performance of each classifier. Here, each row represents the true class and each column the predicted class; correct classifications appear on the diagonal, while off-diagonal elements represent misclassifications.

When examining the low-mass population by itself, where there are only 2 possible classes (WDWD and NSWD), we also evaluate the classifiers' performance using the specificity, sensitivity, Matthews correlation coefficient (MCC), and the area under the receiver operating characteristic (AUROC) curve. In this binary classification task, we define the positive class to be NSWD and the negative class to be WDWD.

The specificity (also known as the true negative rate, TNR) is defined as

$$\text{Specificity} = \frac{\text{TN}}{\text{TN} + \text{FP}}. \quad (12)$$

This metric is an indication of how well the classifier predicts the negative class. Its values range from 0 to 1, with values closer to 1 indicating stronger performance.

Sensitivity (or also known as the true positive rate, TPR, or recall) is defined as

$$\text{Sensitivity} = \frac{\text{TP}}{\text{TP} + \text{FN}}, \quad (13)$$

and quantifies how well the classifier recovers the positive class. As with specificity, values closer to 1 correspond to better performance.

The MCC is defined as:

$$\text{MCC} = \frac{\text{TP} \times \text{TN} - \text{FP} \times \text{FN}}{\sqrt{(\text{TP} + \text{FP})(\text{TP} + \text{FN})(\text{TN} + \text{FP})(\text{TN} + \text{FN})}}, \quad (14)$$

and provides a balanced measure of classification performance. We highlight that the MCC incorporates all four entries of a binary confusion matrix, making it particularly suitable for imbalanced datasets—such as ours, where in the low-mass population, WDWDs are far more numerous than NSWDs. MCC values range from -1 (complete disagreement) through 0 (random performance) to 1 (perfect classification).

Finally, the AUROC is computed as the area under the curve obtained by plotting sensitivity against specificity. It can be interpreted as the probability that the classifier assigns a higher score to a randomly chosen NSWD binary than to a randomly chosen WDWD. An AUROC value of 0.5 corresponds to random guessing, while a value of 1 indicates perfect discrimination.

3. Results

In this section, we begin with a multi-class analysis to characterise the overall separability of the various binary systems that are detectable by LISA in the Milky Way. We then focus on binary classification between the most numerous and also the most challenging classes, (namely the low-mass population of WDWD and NSWD), with the aim of quantifying their separability and evaluating the performance of different machine learning classifiers. After identifying the best-performing classifiers, we proceed to optimise their performance using Bayesian optimisation (see Section A.2) and calibrate their outputs with a Bayes' rule-inspired probability calibration method (see Section A.3). Finally, we analyse which features drive the classification, and we assess the classifier's performance on both a realistic test catalogue and an independent catalogue to evaluate its robustness under LISA-like observational conditions.

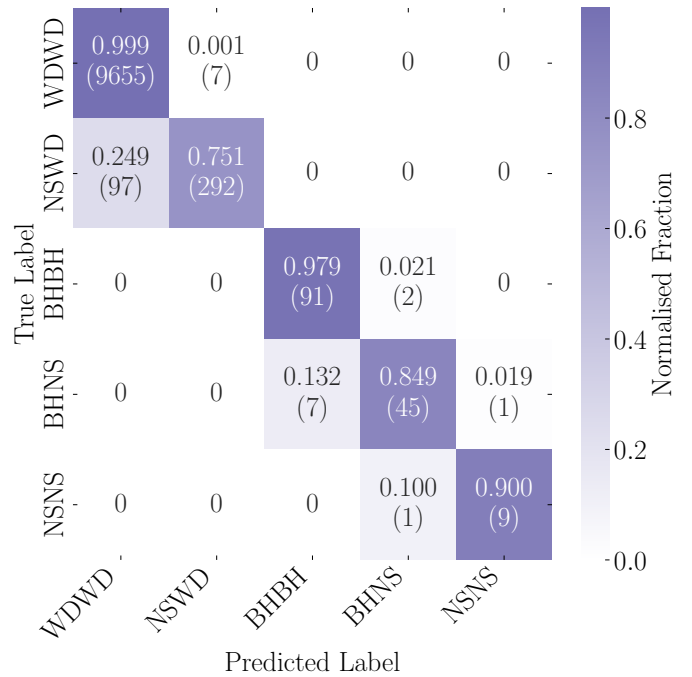


Fig. 2: Confusion matrix of the multi-class XGBoost classifier evaluated on the main catalogue's test set. Each entry is row-normalised and colour-coded by value, with bracketed numbers indicating the absolute counts. The classifier demonstrates strong performance in separating the high-mass binaries (BHBH, BHNS, NSNS), while classification of the low-mass binaries (WDWD, NSWD) remains more challenging. The distinction between WDWD and NSWD is the most difficult, with approximately 25% of NSWD class incorrectly predicted as WDWD.

3.1. Performance on multi-class test set

For the multi-class analysis, we use XGBoost, which showed the strongest performance in preliminary tests. We train it on the main catalogue described in Section 2.2, which includes five binary classes (WDWD, NSWD, BHBH, BHNS, and NSNS), using the training set shown in Fig. 1. We then optimise the model using Bayesian optimisation, with the resulting hyper-parameters listed in Section B. Finally, we evaluate the trained classifier on the main catalogue's test set.

Fig. 2 shows the performance of the XGBoost classifier on the main catalogue's test set. The confusion matrix indicates that the classifier achieves high recall for the high-mass binaries (BHBH, BHNS, and NSNS), with correctly classified fractions exceeding 85% for all three classes. The WDWD systems are also identified with a recall of 99.9%, demonstrating the model's ability to capture the dominant population effectively. However, separating NSWD systems from WDWD binaries proves substantially more challenging: about 25% of true NSWDs are misclassified as WDWDs. This difficulty arises from the close similarity of the gravitational-wave features of WDWD and NSWD binaries within the LISA band. Both classes occupy overlapping regions in frequency, amplitude, and chirp rate, making their signals nearly indistinguishable without an additional measurable handle such as eccentricity (see Fig. 1).

In addition, the extreme class imbalance naturally biases the classifier toward predicting the WDWD class, further increasing NSWD \rightarrow WDWD misclassifications. Although class-balancing

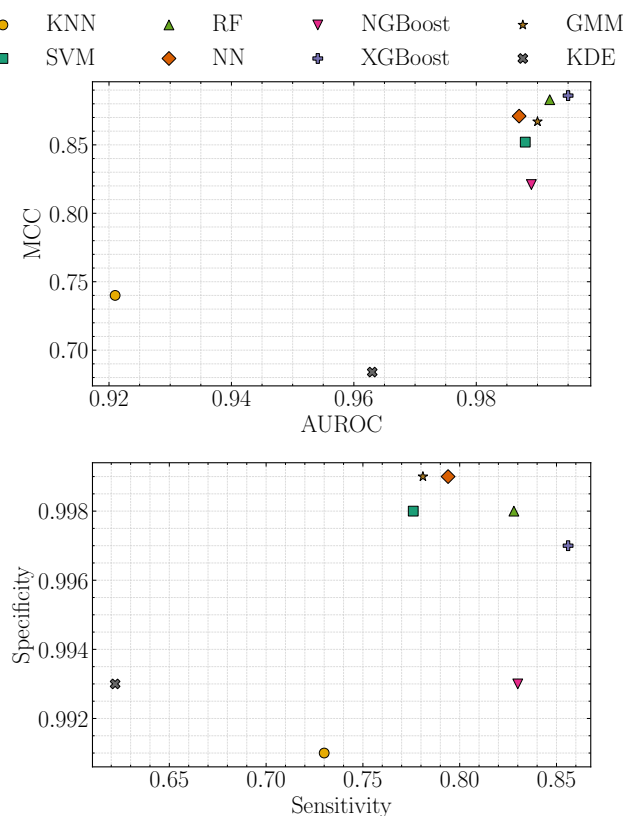


Fig. 3: Performance comparison of machine-learning classifiers evaluated on the test set including NSWD and WDWD binaries only. In both plots, the top-right corner represents the ideal performance.

techniques could mitigate this, they may come at the cost of reduced precision for the dominant WDWD population.

3.2. Performance of classifiers on low-mass population

The multi-class results highlight that separating the most numerous classes, namely WDWD from NSWD systems, is the dominant challenge. Focusing on this low-mass population, we trained the 8 classifiers of Section 2.3 on WDWD and NSWD binaries only and evaluated them on the matching test set. We then calibrated the probability outputs (see Section A.3).

After this calibration, each model provides a continuous probability score p of a system being NSWD rather than WDWD. However, since the two classes show considerable feature-space overlap, the optimal decision threshold s is not guaranteed to be 0.5. To maximize classification performance, we optimized s for each classifier to maximize MCC on the test data. The resulting decision rule is

$$\hat{y} = \begin{cases} 0 \text{ (WDWD)}, & \text{if } p \leq s, \\ 1 \text{ (NSWD)}, & \text{if } p > s, \end{cases} \quad (15)$$

The determined threshold values, listed in Table A.2, varied across methods. Notably, some classifiers (e.g., KNN and NGBoost) required substantial shifts from 0.5. This reflects factors such as class imbalance, feature-space overlap, or the classifier’s intrinsic probability scaling, highlighting the importance of threshold optimization in our specific problem.

The performance of all 8 classifiers on the low-mass population can be seen in Fig. 3.

The figure presents four key metrics introduced in Section 2.3.1: AUROC, MCC, sensitivity, and specificity, with the ideal performance located in the upper-right region of each panel. Across all models, the specificity is very high (typically ≥ 0.99), meaning that WDWD systems are reliably identified. The variation arises primarily in the sensitivity, where KDE and KNN perform noticeably worse. All classifiers achieve AUROC values above 0.92 and positive MCC scores greater than 0.5, confirming that every method performs well above random and retains real discriminatory power despite the strong class imbalance.

Among the tested algorithms, XGBoost, RF, and GMM cluster in the upper-right region of both panels, indicating superior and well-balanced performance compared to the other methods in identifying both classes. Our custom NN performs competitively, showing the effectiveness of classifiers that are capable of capturing non-linear relationships among gravitational-wave features. In contrast, KNN and KDE lie significantly farther from the ideal region, confirming that simple distance-based and non-parametric density estimators struggle with the overlapping, highly imbalanced feature space of compact binaries. The strong performance of decision-tree-based methods (RF, XGBoost) suggests that the gravitational-wave feature space is particularly well suited to classifiers that exploit hierarchical, non-linear decision boundaries. Finally, we note that Bayesian optimisation generally improved the classifiers’ performance, pushing them closer to the upper-right region, although it did not significantly alter their relative ranking.

3.3. Performance of binary classifier - XGBoost

Since XGBoost demonstrated the best overall performance, we now examine its results in more detail to understand the factors behind its effectiveness and the remaining classification challenges. For context and benchmarking, we also compare its performance to the KDE method, which serves as a simple statistical baseline relying purely on the underlying density distributions without learning complex decision boundaries. The optimised hyper-parameters obtained through Bayesian optimisation for the binary XGBoost classifier are listed in

Section B.

The bottom left of Fig. 4 shows the corner plot of the feature distributions for correctly (blue) and incorrectly (red) predicted compact binary systems with XGBoost. Although the overall feature distributions appear complex, the classifier successfully identifies the majority of binary systems correctly. Among the misclassified systems, clustering is evident within specific ranges of certain features, notably f_{GW} , $\log \mathcal{A}_0$, $\log \hat{f}_{\text{GW}}$, and e . In contrast, the angular parameters ($\sin \beta$, $\cos \iota$, λ , ψ , ϕ_0) show no clear structure, with the misclassified systems distributed more randomly—except for λ , where a slight concentration is observed. This behaviour is expected: while ι , ψ , and ϕ_0 are randomly sampled, the sky coordinates follow a Milky Way-like stellar density distribution that peaks toward the Galactic bulge, which can lead to subtle correlations with classification errors, particularly in λ .

The clustering of misclassified systems in specific regions of the parameter space arises primarily from two factors. First, these regions correspond to high source densities in the astrophysical catalogues, so a larger population naturally yields a higher absolute number of errors. Second, the intrinsic properties of WDWD and NSWD binaries overlap significantly in these regions, making them inherently difficult to distinguish. For reference, in our training set the NSWD-to-WDWD ratio exceeds

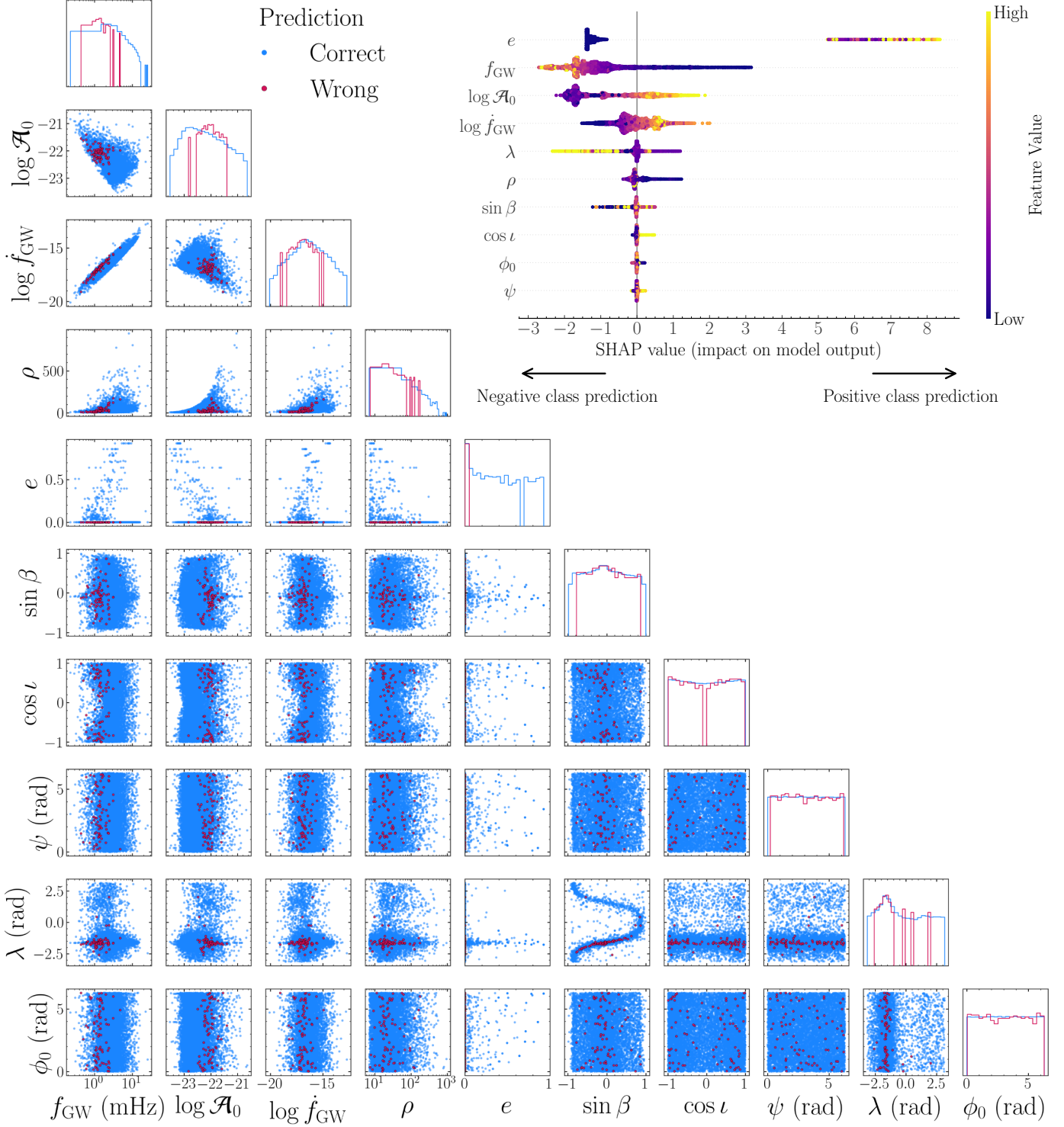


Fig. 4: Feature distributions for correctly (blue) and incorrectly (red) predicted low-mass binary systems (WDWD and NSWD) by XGBoost binary classifier evaluated on the main catalogue’s test set. The inset in the upper-right corner shows a SHAP summary plot illustrating the impact of the ten input features on the classifier’s output for each system in the low-mass component test set. The features are ranked on the y-axis in descending order of average absolute importance. The x-axis shows the SHAP value, indicating the feature’s contribution to the output, where a positive value pushes the prediction towards the positive class (NSWD) and a negative value pushes it towards the other (WDWD). A SHAP value of 0, marked by the vertical grey line, represents the baseline and indicates the feature had no impact on that specific prediction. Each point corresponds to an individual system from the test set, coloured by its normalised feature value, from low (dark blue) to high (yellow).

0.3 at frequencies below $\lesssim 1$ mHz, whereas above ~ 2 mHz the ratio drops to nearly zero. This implies that the error distribution is at least partly driven by underlying astrophysical structure,

though a detailed physical interpretation lies beyond the scope of this work.

3.3.1. Classifier’s interpretability with SHAP

We can further interpret the performance of a machine learning classifier by using SHapley Additive exPlanations (SHAP) (Lundberg & Lee 2017). This is a model interpretation method that utilises the concept of Shapley value in game theory (Shapley et al. 1953). Essentially, SHAP helps to explain how much each input feature contributes to a model’s final prediction. It assigns a numerical value (SHAP value) for each individual prediction, indicating whether that feature increases or decreases the likelihood of a given outcome.

This provides an intuitive way to understand the complex decisions made by the model and may also provide clues as to whether or not the features driving its classifications are physically motivated.

The inset in Fig. 4 on the upper-right plot shows the SHAP summary plot for the binary XGBoost classifier. The features are ranked on the y-axis according to their average absolute SHAP value, indicating their overall importance to the model’s decision. The x-axis represents the SHAP value itself, that is the magnitude and sign of each feature’s contribution to the classification output. Positive values push the prediction towards the NSW class and negative values towards the WD class. Each point corresponds to an individual system in the test set, coloured by the feature’s normalised value. This analysis reveals that the eccentricity e , gravitational-wave frequency f_{GW} , strain amplitude $\log \mathcal{A}_0$, and frequency derivative $\log \dot{f}_{\text{GW}}$ are the most influential features driving the classifier’s predictions. Specifically, systems with lower f_{GW} and higher $\log \mathcal{A}_0$ and $\log \dot{f}_{\text{GW}}$ tend to be classified as NSWs. For eccentricity e , highly eccentric systems are generally classified as NSWs, whereas systems with zero eccentricity are typically identified as WDs. This trend is astrophysically motivated: WDWD binaries are expected to have circular orbits due to tidal circularisation during their common-envelope evolution (e.g. Iben & Livio 1993; Zahn 1977), while NSW systems can retain measurable eccentricities as a result of natal kicks imparted during the supernova event that formed the neutron star (e.g. Igoshev et al. 2021; O’Doherty et al. 2023; Valli et al. 2025).

Other features, such as SNR (ρ) and the angular parameters ($\lambda, \sin \beta, \cos \iota, \psi, \phi_0$), have comparatively smaller impacts on the classifier’s predictions. This is expected, as the SNR ratio is determined by the strain amplitude, gravitational-wave frequency and frequency derivative (see Eq. 7), meaning it does not provide additional independent information once these features are included in the training data. Similarly, the angular parameters in our catalogue are drawn randomly from their respective distributions (see Table 1) for both classes and therefore carry no intrinsic correlation with the binary type. Consequently, these features contribute minimally to the classification process.

3.3.2. XGBoost vs. KDE-based classification

Fig. 5 shows the confusion matrices for XGBoost and KDE on the low-mass population. The KDE method achieves high specificity for WDWD systems (99.3%) but correctly identifies only 62.2% of NSW systems.

In contrast, XGBoost substantially improves performance on the minority class, correctly classifying 85.6% of NSW systems while maintaining excellent specificity (99.7%) for WDWD

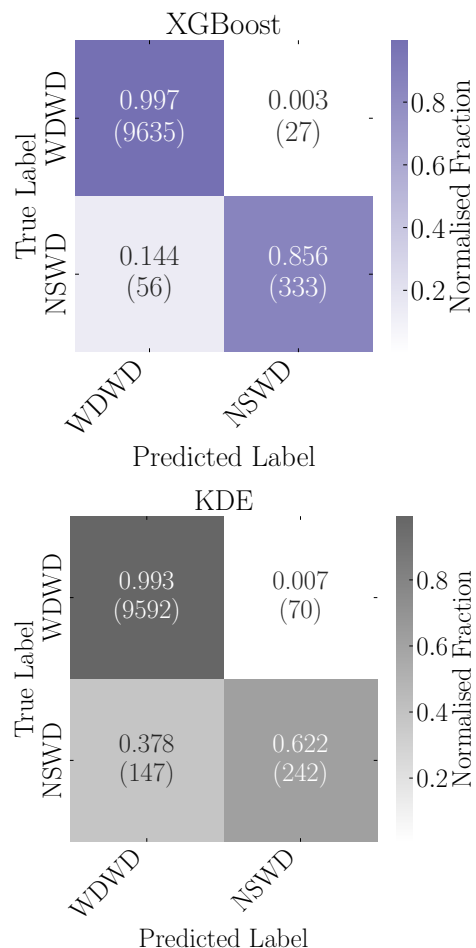


Fig. 5: Confusion matrices evaluated on the low-mass population test set for the XGBoost (purple) and KDE (grey) classifiers. Each entry is row-normalised and colour-coded by value, with bracketed numbers indicating the absolute counts. The results show that XGBoost performs significantly better, correctly predicting 85.6% of NSW systems compared to 62.2% for KDE. For the same population, XGBoost predicts 360 NSW systems, whereas KDE predicts 312.

systems. These results confirm that XGBoost achieves a very balanced separation between the two binary populations, effectively mitigating the bias toward the dominant WDWD class while preserving high specificity. Furthermore, when compared to the multi-class XGBoost classifier, the binary version shows a clear improvement, with 85.6% of NSW systems correctly predicted compared to 75.3% for the multi-class model. This improvement results from the reduced complexity of the classification task: with only two classes, the model can learn cleaner and more effective decision boundaries, and the optimisation procedure is tailored specifically to distinguishing NSW from WDWD binaries.

From this comparison, we show that machine learning approaches trained on mock data outperform classical statistical methods, and that deploying an optimised binary classifier yields better performance than a multi-class classifier. The KDE approach relies on the ratio of class densities estimated from the training sample, however, when the overlap between classes becomes significant, its predictions tend towards randomness. XGBoost, on the other hand, learns hierarchical relationships be-

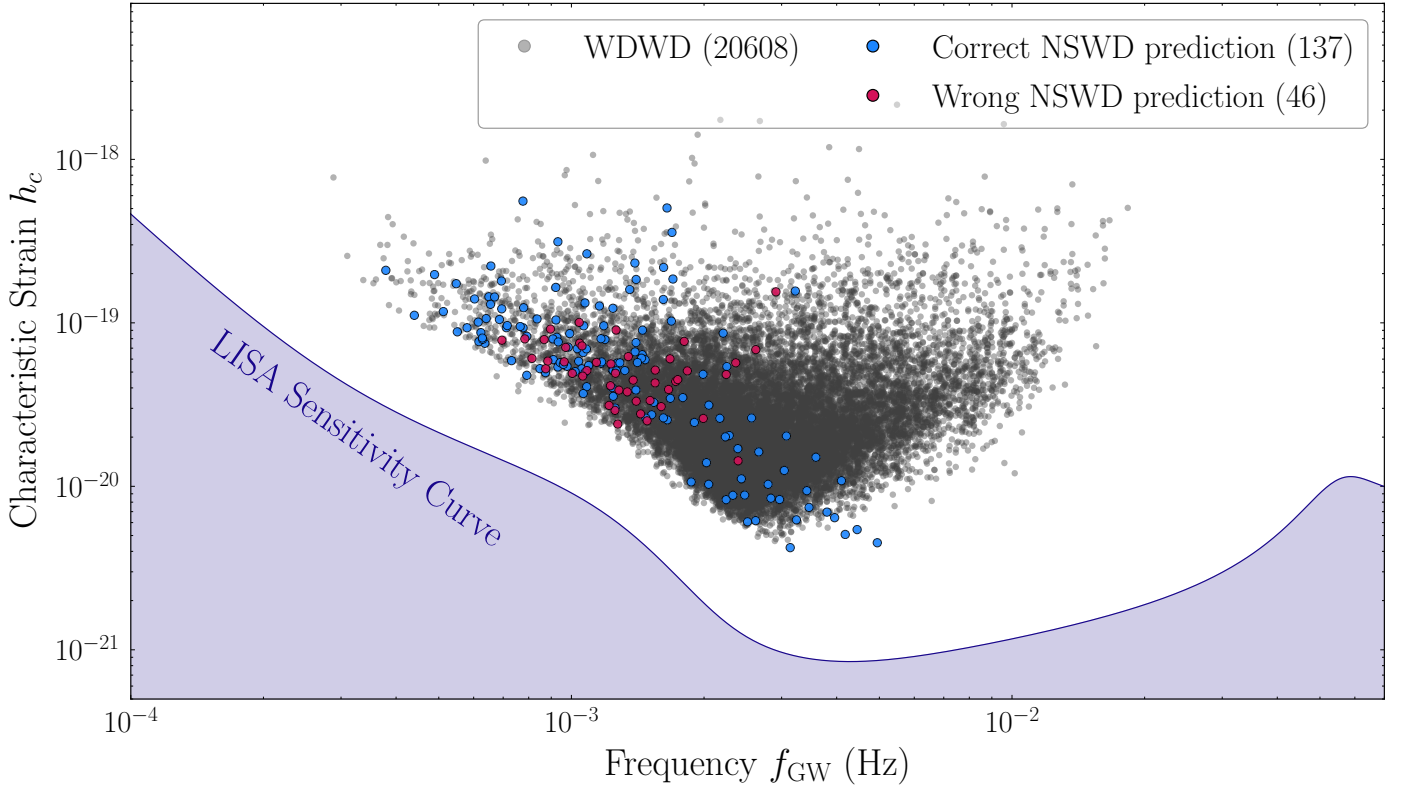


Fig. 6: LISA-detectable Galactic WDWD (grey) populations and NSWD (blue and red) populations of a four-year LISA observation period shown in the gravitational-wave frequency–characteristic strain parameter space, with the LISA sensitivity curve plotted and shaded in purple. The two NSWD scatter plots represent the correctly (blue) and incorrectly (red) predicted NSWD systems by the XGBoost classifier evaluated on the test catalogue.

tween features and is able to capture the underlying structure of the data more effectively. As a result, we demonstrate that state-of-the-art machine learning algorithms can outperform simple statistical classifiers in accurately distinguishing compact binary populations.

3.3.3. Tests with Auxiliary Catalogues

To evaluate the robustness and astrophysical reliability of our best performing classifier, XGBoost, we applied the trained, optimised, and calibrated XGBoost model to the two auxiliary catalogues introduced in Section 2.2.1: (1) the low-mass test catalogue, which is a random realisation of the same astrophysical WDWD and NSWD population models used in our training set and reflects a realistic four-year LISA observation, and (2) the independent catalogue, which contains only WDWD binaries and is generated using a data-driven model rather than the binary population-synthesis models employed during training.

We find that XGBoost’s performance on the low-mass test catalogue remains robust: out of 183 total NSWD systems, only 46 were misclassified. This demonstrates that the model performs significantly better than random classification, even under extreme class-imbalance conditions—where WDWD systems outnumber NSWD systems by a factor of 112—and is able to reliably recover the minority NSWD population in a realistic astrophysical context. In Fig. 6, we show the classification results, and in the discussion below we focus on the performance for NSWD systems, as the classifier consistently achieves high specificity for WDWD systems. The scatter plot highlights the regions where NSWD systems were correctly (blue) and incorrectly (red) clas-

sified. We observe that most misclassified NSWD systems cluster within a specific band of the frequency–characteristic strain plane, between 1 and 2 mHz. While part of this behaviour can be attributed to the intrinsic overlap of WDWD and NSWD binary parameters in this range, we identify the higher source density in this region as the primary driver of the class confusion. A larger NSWD-to-WDWD ratio in that band naturally leads to more misclassifications for statistical reasons, as previously noted for Fig. 4. At higher frequencies, the fraction of correctly classified NSWD systems increases. This is because these NSWD binaries are typically eccentric, and each system contributes multiple harmonics to the frequency–strain plane. The presence of eccentricity-related features makes them easier for the classifier to identify, as also indicated by the SHAP analysis in Fig. 4.

When applying XGBoost to the independent catalogue, we find that the classifier correctly identified all WDWD systems. This demonstrates that even when the underlying astrophysical model differs from that used during training, the classifier still generalises reliably and does not produce spurious NSWD classifications. Since the true Galactic population of compact binaries remains uncertain, it is entirely possible that LISA will observe systems that fall outside the assumptions encoded in current models. The results here suggest that, provided the training set is sufficiently broad and representative, the classifier remains stable under model variation and is therefore likely to retain reliable performance once LISA observations become available.

4. Other Applications: identifying eccentric and Galactic Bulge systems

Beyond distinguishing compact-binary types, we investigate a few additional applications of machine-learning classification to LISA data. Specifically, we explore two such examples: identifying eccentric binaries and identifying millisecond-pulsar–white-dwarf binaries in the Galactic bulge.

4.1. Identification of eccentric systems

Our SHAP analysis in Fig. 4 shows that eccentricity is one of the main features contributing to the classification of binary systems between WDWD and NSWD. However, in reality, this feature may not always be measurable. This could be the case, for example, if only a single harmonic of an eccentric binary is detectable, or because eccentricity is not explicitly included in source-extraction pipelines, as is currently the case. As already noted, currently published LISA global-fit pipelines use circular waveforms, primarily because astrophysical models predict that the vast majority ($\sim 99\%$) of LISA sources will be circular WDWD binaries, and major effort to date has therefore focused on extracting this dominant Galactic population. Still, even with the global fit setup using circular waveforms for Galactic sources, eccentric systems can be identified in the post-processing stage as clusters of correlated circular signals (see Section 2). Here we explore whether our machine-learning classifier can assist in identifying such eccentric systems under these practical constraints. To this end, we conduct two complementary experiments.

In the first experiment, we train the XGBoost classifier to predict the binary type (WDWD or NSWD) using the same feature set as in Table 1, except for leaving out eccentricity. The goal is to assess whether binaries can still be correctly classified based solely on the features available to current global-fit pipelines, which typically assume circular orbits. The results of this analysis, for the main catalogue’s test set, are presented in the top panel of Fig. 7. The classifier correctly identifies 74.8% of NSWD systems, compared to 85.6% when eccentricity was included (in Fig. 5). Although the performance decreases as expected, the results remain encouraging, demonstrating that WDWD and NSWD systems can still be effectively distinguished using the remaining astrophysical parameters alone.

In the second experiment, instead of predicting the binary type, we train the XGBoost classifier to identify whether a system is eccentric or not, using the labels NoEcc for binaries with zero eccentricity and Ecc for binaries with non-zero eccentricity. This is illustrated in the bottom panel of Fig. 7, where the classifier correctly identifies 207 out of 265 eccentric binaries (78.1%) and 9713 out of 9786 (99.3%) non-eccentric binaries. These results show that even without explicitly including eccentricity as an input feature, the classifier can infer its presence indirectly from correlated quantities such as frequency, amplitude, and frequency derivative. This provides a practical way to flag candidate eccentric sources in global-fit analyses, which could then be subject to more detailed, dedicated follow-up.

4.2. Identification of millisecond pulsar binaries in the Galactic bulge

As discussed in Section 3, WDWD and NSWD binaries represent the most difficult classes to disentangle, even with state-of-the-art machine-learning classifiers. Within the NSWD population lies an even more challenging subclass: binaries hosting a millisecond pulsar (MSP) and a low-mass white dwarf companion

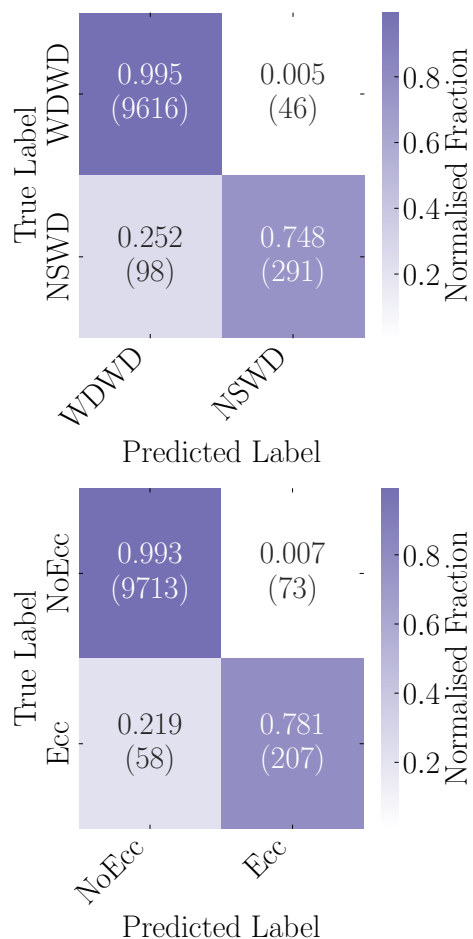


Fig. 7: The confusion matrices for the two experiments described in Section 4.1. Experiment 1 (top) presents the confusion matrix for the evaluation of the XGBoost classifier trained without the feature eccentricity, applied to classify WDWD and NSWD binaries. Experiment 2 (bottom) shows the confusion matrix for the classifier trained without the eccentricity feature but using labels NoEcc (for binaries with zero eccentricity) and Ecc (for binaries with non-zero eccentricity). Each entry is row-normalised and colour-coded by value, with bracketed numbers indicating the absolute counts.

(MSP–WD). These systems form when an old neutron star is spun up through accretion from its companion, producing a rapidly rotating pulsar in a tight, circular orbit with a low-mass WD (for a review, see Lorimer 2008; Tauris 2011). Owing to their low chirp masses and near-zero eccentricities, their gravitational-wave signals are virtually indistinguishable from those of WDWD binaries (Korol & Igoshev 2026).

Identifying such binaries in LISA data would be particularly valuable, as they represent promising candidates for radio follow-up in future multi-messenger studies. This is especially relevant for the potential population of MSP binaries in the Galactic bulge (within the inner 2–3 kpc), where a GeV γ -ray excess has been observed (Goodenough & Hooper 2009; Hooper & Goodenough 2011; Hooper & Linden 2011). The origin of this excess remains one of the most debated questions in high-energy astrophysics—it could arise from dark matter annihilation or from an unresolved population of MSPs (e.g. Hooper 2023). Pulsar searches in this region are notoriously challenging due to strong interstellar scat-

tering, high sky temperature, and severe source confusion, which together obscure the underlying MSP population. LISA, however, offers an alternative probe of this population through its gravitational-wave detections (e.g. Korol & Igoshev 2026).

To explore this possibility, we restricted our catalogue to binaries located within the Galactic bulge and selected only systems with zero eccentricity. This assumption is physically motivated, as these systems form when an old neutron star is spun up through accretion, producing a rapidly rotating pulsar in a tight, nearly circular orbit (Korol & Igoshev 2026). We then applied our XGBoost classifier to this bulge-only subset. The classifier correctly identifies 8727 out of 8742 WDWD systems (99.8%) and 6 out of 11 NSWSD systems (54.5%). Although the identification efficiency for the NSWSD systems remains modest, it is still significantly better than random: given the severe class imbalance, a random classifier would select an NSWSD with a probability equal to its fraction in the sample, which corresponds to 11 systems out of a total of 8753, or approximately 0.13%. Despite these limitations, the results demonstrate that LISA could still identify a fraction of MSP binaries in the Galactic bulge. Even a few such detections would be of considerable interest, as they could confirm the presence of a much larger underlying population and provide valuable targets for coordinated electromagnetic follow-up observations (for details see Korol & Igoshev 2026). However, there remains potential to improve the classification performance.

5. Conclusions

In this study, we investigated the feasibility of classifying Galactic stellar-remnant binaries in LISA data using machine-learning techniques. Our aim was to assess whether different Galactic binary types can be distinguished using only gravitational-wave parameters measured by LISA. Using an XGBoost multi-class classifier, we showed that high-mass binaries (BHBH, BHNS, NSNS) can be readily separated, whereas distinguishing low-mass binaries (WDWD and NSWSD) is substantially more challenging and calls for a classifier specifically optimised for this task. Among the methods tested, XGBoost delivered the best performance for this low-mass population, correctly identifying 85.6% of NSWSD systems despite the severe class imbalance. We further demonstrated that the classifier generalises across population synthesis realizations and data-driven models, successfully identifying WDWD systems generated from a different framework than the one used for training.

We also explored additional astrophysical applications of this approach. First, we showed that the classifier can identify eccentric sources even when eccentricity is not provided explicitly, by learning correlated patterns in other observables. When eccentricity information was removed from the feature set—reflecting the current limitations of LISA global-fit pipelines—the classifier still retained meaningful discriminative power. Second, we applied the classifier to a bulge-restricted catalogue to assess whether LISA could help identify potential MSP-WD binaries in the inner Galaxy. Although classification in this regime remains challenging, the model still identified a non-negligible fraction of NSWSD systems, well above random expectation, demonstrating that machine learning may aid in probing Galactic bulge MSP populations.

In summary, our results demonstrate that modern ensemble-based machine-learning algorithms—particularly gradient-boosting methods—offer strong potential for source classification in LISA data as a first step toward the astrophysical interpretation of quasi-monochromatic LISA sources. We have shown that such classifiers can be applied to multiple astrophysical aspects—from

distinguishing compact-binary types, to identifying eccentric systems, to pinpointing candidates of rare populations—illustrating how machine learning can facilitate the full scientific potential of LISA.

Acknowledgements. We thank Silvia Toonen and Tom Wagg for providing the binary population data, and Natalia Korsakova, Stephen Justham, and Christopher Moore for helpful discussions. We also thank the members of the Origins Data Science Lab, in particular Nicole Hartman, Annalena Kofler and Lukas Heinrich, for their feedback on machine learning aspects of this work and valuable suggestions.

This research was supported by the Munich Institute for Astro-, Particle and BioPhysics (MIAPbP) which is funded by the Deutsche Forschungsgemeinschaft (DFG, German Research Foundation) under Germany’s Excellence Strategy – EXC-2094 – 390783311.

References

- Amaro-Seoane, P., Andrews, J., Arca Sedda, M., et al. 2023, *Living Reviews in Relativity*, 26, 2
- Auclair, P., Bacon, D., Baker, T., et al. 2023, *Living Reviews in Relativity*, 26, 5
- Bailer-Jones, C. A. L., Fouesneau, M., & Andrae, R. 2019, *Monthly Notices of the Royal Astronomical Society*, 490, 5615–5633
- Barausse, E., Berti, E., Hertog, T., et al. 2020, *General Relativity and Gravitation*, 52, 81
- Berbel, M., Miravet-Tenés, M., Sharma Chaudhary, S., et al. 2024, *Classical and Quantum Gravity*, 41, 085012
- Bergstra, J. & Bengio, Y. 2012, *Journal of Machine Learning Research*, 13, 281
- Breiman, L. 2001, *Mach. Learn.*, 45, 5–32
- Breivik, K., Coughlin, S., Zevin, M., et al. 2020, *ApJ*, 898, 71
- Broekgaarden, F. S., Berger, E., Neijssel, C. J., et al. 2021, *MNRAS*, 508, 5028
- Broekgaarden, F. S., Berger, E., Stevenson, S., et al. 2022, *MNRAS*, 516, 5737
- Chen, T. & Guestrin, C. 2016, in *Proceedings of the 22nd ACM SIGKDD International Conference on Knowledge Discovery and Data Mining, KDD ’16* (New York, NY, USA: Association for Computing Machinery), 785–794
- Chen, W.-C., Liu, D.-D., & Wang, B. 2020, *ApJ*, 900, L8
- Colpi, M., Danzmann, K., Hewitson, M., et al. 2024, *arXiv e-prints*, arXiv:2402.07571
- Cortes, C. & Vapnik, V. 1995, *Mach. Learn.*, 20, 273–297
- Cover, T. & Hart, P. 1967, *IEEE Transactions on Information Theory*, 13, 21
- Deng, S., Babak, S., Le Jeune, M., et al. 2025, *Phys. Rev. D*, 111, 103014
- Duan, T., Avati, A., Ding, D. Y., et al. 2020, *NGBoost: Natural Gradient Boosting for Probabilistic Prediction*
- Garnett, R. 2023, *Bayesian optimization* (Cambridge University Press)
- Goodenough, L. & Hooper, D. 2009, *arXiv e-prints*, arXiv:0910.2998
- Hooper, D. 2023, *SciPost Phys. Proc.*, 006
- Hooper, D. & Goodenough, L. 2011, *Physics Letters B*, 697, 412
- Hooper, D. & Linden, T. 2011, *Phys. Rev. D*, 84, 123005
- Iben, Jr., I. & Livio, M. 1993, *PASP*, 105, 1373
- Igoshev, A. P., Chruslinska, M., Dorozsmai, A., & Toonen, S. 2021, *MNRAS*, 508, 3345
- Karnesis, N., Babak, S., Pieroni, M., Cornish, N., & Littenberg, T. 2021, *Phys. Rev. D*, 104, 043019
- Katz, M. L., Danielski, C., Karnesis, N., et al. 2022, *MNRAS*, 517, 697
- Katz, M. L., Karnesis, N., Korsakova, N., Gair, J. R., & Stergioulas, N. 2025, *Phys. Rev. D*, 111, 024060
- Korol, V., Buscicchio, R., Pakmor, R., et al. 2024a, *A&A*, 691, A44
- Korol, V., Hallakoun, N., Toonen, S., & Karnesis, N. 2022, *MNRAS*, 511, 5936
- Korol, V. & Igoshev, A. 2026, *A&A*, 705, A154
- Korol, V., Igoshev, A. P., Toonen, S., et al. 2024b, *MNRAS*, 530, 844
- Korol, V., Rossi, E. M., Groot, P. J., et al. 2017, *MNRAS*, 470, 1894
- Lackeos, K., Littenberg, T. B., Cornish, N. J., & Thorpe, J. I. 2023, *A&A*, 678, A123
- Lamberts, A., Blunt, S., Littenberg, T. B., et al. 2019, *MNRAS*, 490, 5888
- Lamberts, A., Garrison-Kimmel, S., Hopkins, P. F., et al. 2018, *MNRAS*, 480, 2704
- Lau, M. Y. M., Mandel, I., Vigna-Gómez, A., et al. 2020, *MNRAS*, 492, 3061
- Li, Z., Chen, X., Ge, H., Chen, H.-L., & Han, Z. 2023, *A&A*, 669, A82
- LISA Science Requirements Document. 2018, *LISA Science Requirements Document*, Tech. Rep. ESA-L3-EST-SCI-RS-001, ESA, www.cosmos.esa.int/web/lisa/lisa-documents/
- Littenberg, T. B. & Cornish, N. J. 2023, *Phys. Rev. D*, 107, 063004
- Lorimer, D. R. 2008, *Living Reviews in Relativity*, 11, 8
- Lundberg, S. M. & Lee, S.-I. 2017, 4768–4777
- Middleton, H., Kolitsidou, P., Klein, A., et al. 2025, *arXiv e-prints*, arXiv:2507.11442
- Moore, C. J., Finch, E., Klein, A., et al. 2024, *MNRAS*, 531, 2817

- Muehleisen, R. T. & Bergerson, J. 2016
- Nelemans, G. & Tout, C. A. 2005, MNRAS, 356, 753
- Nelemans, G., Verbunt, F., Yungelson, L. R., & Portegies Zwart, S. F. 2000, A&A, 360, 1011
- Nelemans, G., Yungelson, L. R., & Portegies Zwart, S. F. 2001, A&A, 375, 890
- Nissanke, S., Vallisneri, M., Nelemans, G., & Prince, T. A. 2012, ApJ, 758, 131
- O'Doherty, T. N., Bahramian, A., Miller-Jones, J. C. A., et al. 2023, MNRAS, 521, 2504
- Pedregosa, F., Varoquaux, G., Gramfort, A., et al. 2011, Journal of Machine Learning Research, 12, 2825
- Peters, P. C. & Mathews, J. 1963, Physical Review, 131, 435
- Popov, S., Müller, B., & Mandel, I. 2025, New Astronomy Reviews, 101, 101734
- Portegies Zwart, S. F. & Verbunt, F. 1996, A&A, 309, 179
- Rajamuthukumar, Abinaya Swaruba, Korol, Valeriya, Stegmann, Jakob, et al. 2025, A&A, 704, A156
- Riley, J., Agrawal, P., Barrett, J. W., et al. 2022, ApJS, 258, 34
- Schafer, R. W. 2011, IEEE Signal Processing Magazine, 28, 111
- Sesana, A., Lamberts, A., & Petiteau, A. 2020, MNRAS, 494, L75
- Seto, N. 2001, Phys. Rev. Lett., 87, 251101
- Shahriari, B., Swersky, K., Wang, Z., Adams, R. P., & de Freitas, N. 2016, Proceedings of the IEEE, 104, 148
- Shapley, L. S. et al. 1953
- Silverman, B. W. & Jones, M. C. 1989, International Statistical Review / Revue Internationale de Statistique, 57, 233
- Snoek, J., Larochelle, H., & Adams, R. P. 2012, in Advances in Neural Information Processing Systems, ed. F. Pereira, C. Burges, L. Bottou, & K. Weinberger, Vol. 25 (Curran Associates, Inc.)
- Strub, S. H., Ferraioli, L., Schmelzbach, C., Stähler, S. C., & Giardini, D. 2024, Phys. Rev. D, 110, 024005
- Tang, P., Eldridge, J. J., Meyer, R., et al. 2024, MNRAS, 534, 1707
- Tauris, T. M. 2011, in Astronomical Society of the Pacific Conference Series, Vol. 447, Evolution of Compact Binaries, ed. L. Schmidtbreick, M. R. Schreiber, & C. Tappert, 285
- Thiele, S., Breivik, K., Sanderson, R. E., & Luger, R. 2023, ApJ, 945, 162
- Toonen, S., Hollands, M., Gänsicke, B. T., & Boekholt, T. 2017, A&A, 602, A16
- Toonen, S., Nelemans, G., & Portegies Zwart, S. 2012, A&A, 546, A70
- Toonen, S., Perets, H. B., Igoshev, A. P., Michaely, E., & Zenati, Y. 2018, A&A, 619, A53
- Valli, R., de Mink, S. E., Justham, S., et al. 2025, arXiv e-prints, arXiv:2505.08857
- van der Sluys, M. V., Verbunt, F., & Pols, O. R. 2006, A&A, 460, 209
- Vigna-Gómez, A. 2025, A&A, 701, L3
- Wagg, T., Broekgaarden, F. S., de Mink, S. E., et al. 2022, ApJ, 937, 118
- Wagg, T., Dalcanton, J. J., Renzo, M., et al. 2025, AJ, 170, 192
- Zahn, J.-P. 1977, A&A, 57, 383

Appendix A: Details of implementation

Appendix A.1: Binary Classifiers

In this section, we elaborate on the methods and parameter choices for the binary classifiers not discussed in the main text. Table A.1 lists the optimisation and probability calibration techniques applied to each model. For most classifiers, Bayesian optimisation is used to identify the optimal set of hyper-parameters. The exceptions are as follows. For the KDE method, we used a simple grid search to serve as a baseline. For the KNN classifier, we selected $k = 5$ in order to optimize its F_1 score¹. The configurations of the NN and NGBoost were determined based on preliminary experimentation and design considerations.

For our custom NN, we employed a focal loss function to address class imbalance. To further help with this challenge, we generated an additional 100 NSWd samples for each NSWd binary system by sampling from the uncertainties derived from the Fisher information matrix. Each NSWd data point was weighted inversely proportional to the number of occurrences of its source system to reduce bias introduced by multiple harmonics originating from the same binary. The network architecture consists of an input layer, six hidden layers, and an output layer. ReLU activations are used between layers, and 30% dropout was applied in the first three hidden layers and subsequently 20% dropout was applied to the last three hidden layers the network. The final output layer employs a sigmoid activation. Training was performed for 100 epochs with a batch size of 128 for both training and inference.

For NGBoost, we used the default implementation without additional modifications. Lastly, for our custom GMM, we followed the approach described in Bailer-Jones et al. (2019). We incorporated custom class priors based on the relative abundance of WDWD and NSWd systems in the Milky Way, set to $\{0 : 0.96, 1 : 0.04\}$. Since the GMM classifier already incorporates prior information in its probability estimates, no additional probability calibration was applied.

The optimised decision threshold values, as described in Section 3.2, which set the required predicted probabilities before classifying a system as NSWd, are shown in Table A.2.

Appendix A.2: Bayesian Optimisation

All of our classifiers have one or more hyper-parameters, which are configuration variables that govern the structure and learning behaviour of a model, but are not directly learned from the training data. Examples include the number of trees in a RF, the learning rate in gradient boosting algorithms, or the kernel type in an SVM. Traditional hyper-parameter optimisation often involves exhaustive grid searches, which systematically evaluate all possible combinations within a predefined parameter space. However, this is often inefficient and random searches could perform better than grid searches, especially when the dimensionality and complexity increases (Bergstra & Bengio 2012).

In contrast, Bayesian Optimisation (Garnett 2023) frequently produces better results with fewer evaluations (Snoek et al. 2012; Shahriari et al. 2016). Its usage and popularity have risen considerably in recent years, to the extent that widely adopted libraries such as `scikit-learn` now provide dedicated functions for Bayesian Optimisation (Pedregosa et al. 2011), which is what we used for our optimisation process.

¹ $F_1 = \frac{2TP}{2TP+FP+FN}$

Appendix A.3: Bayes' Rule Probability Calibration

The predicted probability from classifiers is not necessarily calibrated to represent the actual probability of the underlying data. In practice, it is often an algorithmic confidence rather than a Bayesian probability (see Berbel et al. 2024, for an example on RF classifiers). Therefore, we applied probability calibration. A traditional probability calibrator learns a direct mapping from model scores to calibrated probabilities using a held-out dataset. This approach implicitly assumes that the observed data are noise-free, and all uncertainty lies in the model output, which is reduced through calibration (Muehleisen & Bergerson 2016). In addition, when class imbalance is severe, as in our case, the probability will be heavily skewed towards 0 or 1, even after calibrating. Hence, we adapted the calibration method described in Berbel et al. (2024) to obtain probabilities that both incorporate uncertainty and remain well-defined. This method uses Bayes' rule to calibrate the classifier's output into an informative probability.

We begin by defining $S(\mathbf{X})$ as the distribution of classifier score outputs, where \mathbf{X} denotes the feature inputs from a held-out dataset. In practice, this corresponds to the `predict_proba` function of most `scikit-learn` classifiers. To model the distribution of scores conditional on the true label, we split the outputs into two groups: those from the positive class $S(\mathbf{X} | y = 1)$ and those from the negative class $S(\mathbf{X} | y = 0)$. By fitting a kernel density estimator we obtain smooth approximations of the class-conditional probabilities: $p(S | y = 1)$ and $p(S | y = 0)$. These densities are further stabilised using a Savitzky–Golay smoothing filter to reduce noise (Schafer 2011). We also compute empirical class priors, $\pi_1 = P(y = 1 | \mathbf{X})$ and $\pi_0 = P(y = 0 | \mathbf{X})$, essentially assuming the priors to be the distribution of classes in the held-out dataset. Lastly, applying Bayes' Theorem for class 1:

$$P(y = 1 | S) = \frac{p(S | y = 1)\pi_1}{p(S | y = 1)\pi_1 + p(S | y = 0)\pi_0}, \quad (\text{A.1})$$

and similarly can be achieved for $P(y = 0 | S)$. This posterior is computed on a grid of score values in $[0, 1]$, yielding a calibrated mapping from uncalibrated classifier scores to probabilities. Finally, we interpolate this mapping to construct a continuous calibration function, which can then be applied to unseen test-set scores to obtain calibrated probabilities.

Appendix B: Hyper-parameter Tuning for XGBoost

The results obtained for the hyper-parameters after using Bayesian optimisation for XGBoost classifier in the multi-class classification case can be found in Table B.1 and the binary classification case can be found in Table B.2.

We briefly summarize the tuned parameters here. The parameter `max_depth` limits the maximum depth of each decision tree, preventing overfitting. `n_estimators` defines the number of boosting rounds, while `learning_rate` scales the contribution of each tree to improve generalisation. `colsample_bytree` and `subsample` specify the fraction of features and training samples used per tree, introducing randomness to reduce overfitting. `gamma` sets the minimum loss reduction required for further partitioning, and `min_child_weight` controls the minimum sum of instance weights in a child node, acting as another form of regularisation.

For further reading, a detailed description of all available parameters and their tuning guidelines can be found in the official

Table A.1: Summary of the hyper-parameter optimisation and probability calibration methods used for each classifier. In general, Bayesian optimisation is adopted as our standard hyper-parameter optimisation approach, and Bayes’ rule probability calibration is used as the primary calibration method.

Classifier	Hyper-parameter optimisation technique	Probability calibration technique
KDE	Grid Search	No calibration
KNN	$k = 5$	Bayes’ rule probability calibration
SVM	Bayesian Optimisation	Bayes’ rule probability calibration
RF	Bayesian Optimisation	Bayes’ rule probability calibration
NN	N.A.	No calibration
NGBoost	N.A.	No calibration
GMM	Bayesian Optimisation	No calibration
XGBoost	Bayesian Optimisation	Bayes’ rule probability calibration

Table A.2: Summary of the optimised score thresholds used to determine each classifier’s positive and negative predictions based on Eq. (15).

Classifier	Optimised score threshold
KDE	0.500
KNN	0.175
SVM	0.560
RF	0.368
NN	0.479
NGBoost	0.128
GMM	0.469
XGBoost	0.497

Table B.1: Summary of sampled hyper-parameters obtained from Bayesian optimisation for the multi-class XGBoost classifier and their assumed priors. $\mathcal{U}(a, b)$ denotes a uniform distribution between a and b , while $\mathcal{U}_{\log}(a, b)$ denotes a log-uniform distribution between a and b , i.e. $\log x \sim \mathcal{U}(\log a, \log b)$. Parameters not listed in the table were fixed to their default values.

Hyper-parameter	Prior	Value
colsample_bytree	$\mathcal{U}(0.5, 1)$	0.61317
learning_rate	$\mathcal{U}_{\log}(10^{-3}, 0.3)$	0.052226
n_estimators	$\mathcal{U}(50, 1000)$	701
max_depth	$\mathcal{U}(3, 12)$	10

Table B.2: As Table B.1 but for the binary XGBoost classifier for the low-mass population.

Hyper-parameter	Prior	Value
colsample_bytree	$\mathcal{U}(0.5, 1)$	0.85172
learning_rate	$\mathcal{U}_{\log}(10^{-3}, 0.3)$	0.0019931
n_estimators	$\mathcal{U}(50, 3000)$	2626
max_depth	$\mathcal{U}(3, 24)$	11
gamma	$\mathcal{U}(0, 5)$	2.0579
min_child_weight	$\mathcal{U}(1, 10)$	5
subsample	$\mathcal{U}(0.5, 1)$	0.99617

XGBoost documentation: <https://xgboost.readthedocs.io/en/stable/parameter.html>